 CMC, vol.17, no.2, pp.149-174, 2010

Modeling and Characterization of Grain Scale Strain Distribution in Polycrystalline Tantalum

C. A. Bronkhorst[1,2], A. R. Ross[3], B. L. Hansen[1]
E. K. Cerreta[2] and J. F. Bingert[2]

Abstract: A common sample geometry used to study shear localization is the "tophat": an axi-symmetric sample with an upper "hat" portion and a lower "brim" portion. The gage section lies between the hat and brim. The gage section length is on the order of 0.9 mm with deformation imposed through a Split-Hopkinson Pressure Bar system at maximum top-to-bottom velocity in the range of 10-25 m/sec. Detailed metallographic analysis has been performed on sections of the samples to quantify the topology and deformation state of the material after large deformation shear. These experiments performed with polycrystalline tantalum have been modeled using a multi-scale polycrystal plasticity approach. A Voronoi tessellation based microstructural model and a coupled thermo-mechanical elasto-viscoplastic crystal plasticity model was used. The crystal plasticity model allowed for slip to occur on the twelve $\{110\}\langle 111\rangle$ and twelve $\{112\}\langle 111\rangle$ slip systems. Three numerical models were produced using three different realizations of initial crystallographic texture distribution within the same morphological microstructure and the results presented. The detailed metallographic analysis of the deformed sample shear zone produced an estimate for the strain profile within that region and these results are compared directly to the three numerical simulation results. Although the models predict a stress response which is greater than that observed experimentally, the local strain response compares very well with the results of the metallographic analysis.

Keywords: Shear localization; Microstructure; Crystal Plasticity; Dynamic; Damage

[1] Theoretical Division, Los Alamos National Laboratory, Los Alamos, NM 87545, LA-UR-09-06367

[2] Corresponding author. Tel.: +1 505 665 0122; fax: +1 505 665 5926. E-mail address: cabronk@lanl.gov.

[3] Materials Science and Technology Division, Los Alamos National Laboratory, Los Alamos, NM 87545, LA-UR-09-06367

1 Introduction

The problem of predicting the dynamic damage evolution and failure of polycrystalline metallic materials which do so by ductile processes (i.e. porosity, localization) remains a challenge. The classical problem of porosity based material damage (Gurson, 1977; Tvergaard, 1981, 1982; Tvergaard and Needleman, 1984; Addessio and Johnson, 1993; Zavaliangos and Anand, 1993; Haghi, 1995) and failure is one of evolving length scales. Pores nucleate at locations in the material which are determined by a combination of the intensity of the external loading and the statistical distribution of microstructural based defects and/or stress concentrators (e.g. grain boundaries, inclusions, intersections of twin planes, misorientation related plastic strain incompatibility, dislocation sub-cells). These nucleation events must necessarily occur at atomic and sub-grain length scales and are heavily dependent upon details of the microstructure since that is the sole source of heterogeneity. Once a field of nucleated pores exists, continued damage evolution favors the growth of existing pores over nucleation of new sites. At this point, the pores are still generally sub-grain in size. Within this regime of response, the rate sensitivity of the material's plastic response is believed to be a rate controlling mechanism. As the pores continue to grow in size, the stress fields of the individual pores begin to intersect and individual pores begin to join by a process of localized deformation based coalescence. At this point, the individual pores become as large or larger than the average grain size. This localized field connecting individual pores and contributing to the damage process can be across a ligament between pores of several average grain sizes. At this stage accelerations can be large and inertial effects play a role in limiting rates of deformation (Tong and Ravichandran, 1995; Weinberg et al., 2006; Czarnota et al., 2008).

It is within this context that we wish to examine the way in which metallic polycrystals deform and how their microstructures evolve with deformation. We do this through the use of both computational models employing physically based single crystal constitutive models applied through synthetic numerical microstructures and new experimental techniques to quantify granular level deformation response. Such an approach acknowledges that damage and failure processes are influenced not only by the mean response of a material, but also the evolving field statistics. This general effort has been the topic of studies in the recent past.

Lebensohn et al. (2009) have recently presented work in which they have used both a modified form of the visco-plastic self consistent (Lebensohn and Tomé, 1993) model to account for the effects of voids in a homogenized way and an FFT technique (Lebensohn, 2001) where a polycrystal aggregate containing 5% porosity is examined. The results of both polycrystal plasticity techniques is compared directly to plastic flow surfaces of Gurson (1977) and Leblond et al. (1994) mod-

els. They found that the FFT model which accounts for a distribution of porosity within the polycrystal predicts plastic flow stress which is smaller for all values of stress triaxiality than the unit cell models of Gurson and Leblond et al. The authors attribute this to the strong void to void interaction possible in the FFT technique which cannot be accounted for by the unit cell or homogenized polycrystal models accounting for porosity. Barton et al. (2009) have also performed direct numerical simulations on polycrystalline aggregates to represent the structural transformation response of materials (solid-solid phase transformations, twinning). These techniques are able to lend important insights into the inhomogeneous response of such materials.

Vogler and Clayton (2008) performed experiments and two-dimensional polycrystal calculations of shock loaded WHA material which included representation of failure of interfaces between grain and phase boundaries via a cohesive zone model. The single crystal model proposed by the authors is based upon slip processes and uses a conventional power law relationship for the flow rule. Finite elasticity is accounted for in the shock processes through a polynomial free energy potential relationship. The model is also fully thermo-mechanically coupled. The interfacial fracture model employed is one which is based upon a traction criterion for the strength of an interface accounting for both normal and shear components. The models are used to simulate the response of a 2D – 150 μm RVE of the WHA material to shock loading. Results for five different simulations using different combinations of flyer velocity and microstructure configurations were presented – consistent with the five experiments presented. Free surface velocity profiles for both experiments and simulations were presented but substantial differences existed upon comparison. This suggests that substantial work remains in properly understanding and quantifying the statistics of the damage and failure process under dynamic or shock loading conditions.

Schroeter and McDowell (2003) presented displacement field measurement results made on the surface of both simple compression and thin-walled tube torsion specimens. A high resolution grid was applied to the surface of both of these experimental configurations and magnified images taken of the surfaces during the deformation process. The deformation field was then computed directly from image correlation of the deformed grid patterns. The results showed that the local deformation field was highly heterogeneous from not only the aggregate characteristics of the material but that intragranular localized deformation was also observed. The degree of heterogeneity in the deformation fields was measured to be much greater in the case of compression than torsion. Clayton et al. (2002) performed direct polycrystal simulations for the case of compression and a digitally replicated FEM microstructure was produced. Conventional crystal plasticity theory was used

to represent the single crystal response. The authors reported that significant discrepancy existed between the experimental and simulated deformation field results. This is perhaps an indication of the importance of substructural development at the single crystal level leading to sub-granular deformation fields which were not adequately represented by a classical continuum based single crystal model. Clayton and McDowell (2003) present interesting results of calculations performed on a 2D OFHC Cu microstructure constructed from three-node linear plane strain elements. They then assigned crystallographic orientations to the grains either randomly or so that the misorientation angle across a grain boundary did not exceed 15 degrees. The 2D model was then deformed in plane strain compression, plane strain tension, and simple shear. The stress state was calculated at grain boundary elements, triple point elements, and in the bulk crystal elements. The results showed that stress heterogeneity was greater when initial grain orientations were assigned randomly. It was also greater in the grain boundary and triple point elements than those composing the bulk of the grain. The coefficient of variation $(sd(x)/|\bar{x}|)$ for the hydrostatic stress was much less than 1.0 for the bulk material while that for the grain boundary and triple point elements was much greater than 1.0 (especially for shear).

Cheong and Busso (2004, 2006) presented direct numerical simulation results for tensile tests performed on specialized two dimensional microstructural samples containing grains several mm in size. The first study was performed using the experimental results of copper by Delaire (1999). The second study used experimental results of Zhang and Tong (2004) performed with Al-5%Mg. The authors used a single crystal constitutive model which employed edge and screw dislocation densities as the basic internal state variables which govern slip system deformation resistance. The constitutive model material parameters for copper and Al-5%Mg were evaluated against single crystal deformation experiments. The authors found for both materials and microstructures that in order to match the experimental stress-strain responses of the two-dimensional tensile tests that a distribution of intragranular misorientation with maximum angle of 6% was required for the initial state of the large grains. The source of this misorientation heterogeneity was argued to be the initial dislocation structure of the material. The added geometric resistance offered by the distributed misorientation was necessary to quantitatively match the experimental results. The study of Al-5%Mg also included quantitative comparisons of strain profiles along a line down the center of the specimen. The simulations were able to predict strain localization which occurred experimentally in the largest grain within the sample. The predicted localization was too severe without including initial misorientation distribution within the simulated grains and an increase in hardening rate. As a result, both the strain profile and the stress-strain

response were not able to be simultaneously predicted. Some preliminary results were also presented which suggested that the influence of misorientation is unique to very large grain two dimensional samples.

In like fashion, Kalidindi et al. (2004) presented experimental and direct simulations of aluminum columnar grain samples exposed to plane strain compression deformation to moderate strain levels. The cross-sectional grain size was very large so the influence of grain boundaries was much smaller than for more typically sized microstructures. They were able to compare microstructural evolution results between both the simulated and experimental microstructures. The simulations were able to represent reasonably well the experimental results. Unfortunately the experimental and simulated stress-strain responses were not presented for comparison purposes.

The thrust of this work is to present an analysis of recent grain level aspect ratio measurements of Ross (2008) made on a recovered sample of forced shear experiments presented in a previous publication by Bronkhorst et al. (2006). This analysis is then used to compare directly to simulations of one of these experiments using direct polycrystal representation of the shear zone section. Section two of this paper presents an overview of the experimental procedures used by Ross (2008). In section three we outline the essential features of the coupled thermo-mechanical elasto-viscoplastic single crystal constitutive model previously reported by Bronkhorst et al. (2007) and the numerical representation of the axi-symmetric forced shear experiment geometry with polycrystal representation of the shear zone. Both experimental and numerical results are presented in section four. The results are discussed in section five followed by the conclusion in section six.

2 Experimental Procedures

The work presented here uses material and samples from deformation experiments which have been previously reported on by Bronkhorst et al. (2006). These were forced shear experiments of axi-symmetric geometry and are shown schematically in Fig. 1. The forced shear samples of tantalum material were deformed dynamically in a Split-Hopkinson Pressure Bar System at different rates of deformation and the top-to-bottom displacement and top-surface stress were measured as a function of time. One of the experiments presented by Bronkhorst et al. (2006) will be focused on here (Test 1356, 298 K initial temperature, 83 kPa pressure, 8.89 cm striker length). The dynamic displacement and top surface stress results are given in Fig. 2. Ross (2008) has recently performed detailed metallographic analysis and nano-indentation hardness measurements on the above named deformed and recovered sample. We will use and analyze the results of granular aspect ratio measurements on that sample from Ross to arrive at an approximate measure of final

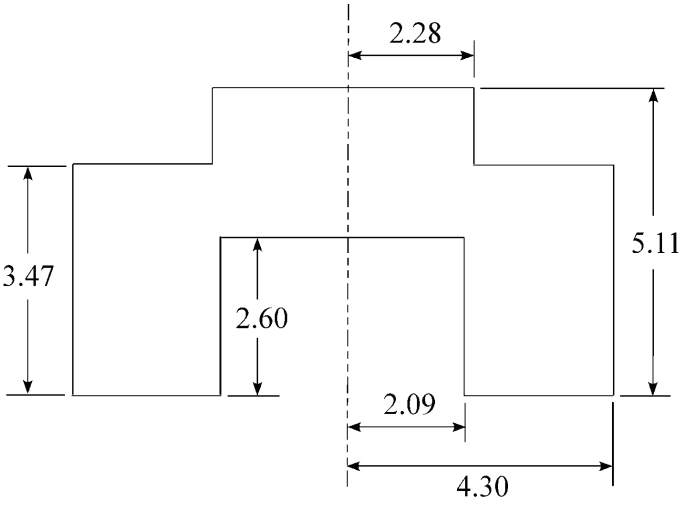

Figure 1: Schematic representation of the cross-sectional geometry of the forced shear sample. The dimensions are in mm.

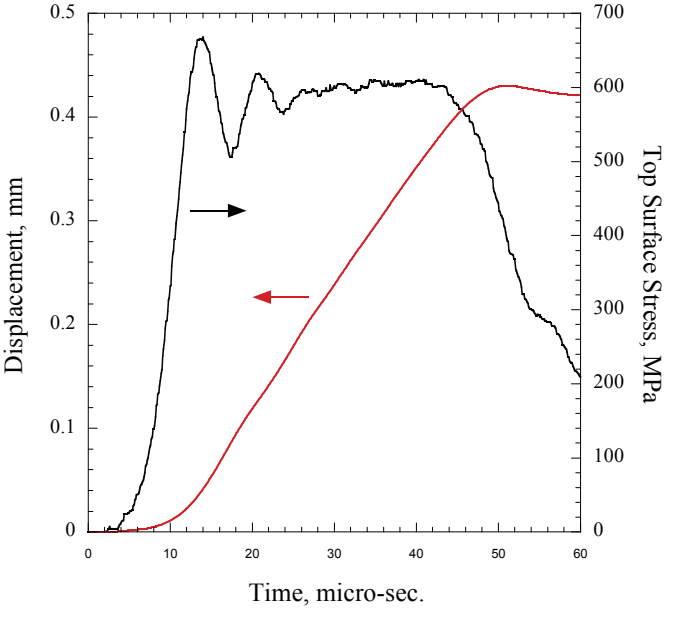

Figure 2: Experimental top-to-bottom surface displacement and top surface stress response for the forced shear experiment.

strain field in the shear zone of this sample.

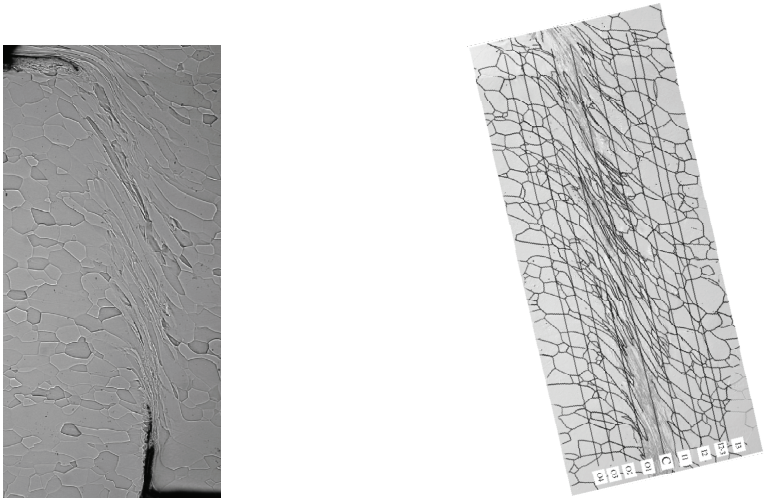

(a) (b)

Figure 3: (a) Metallographic section image of the deformed and recovered sample examined for this study. (b) Digitized shear zone region highlighting the grain boundary structure and used to quantify the deformation profile. Note that measurements were not taken along line I2-3.

The samples were prepared with standard metallographic methods (details can be found in Ross (2008)). After physical preparation, digital micrographs were taken of the shear zone of the sectioned sample and image pre-processing performed. The metallographic images were then used to produce traces of the grain boundaries throughout the image, and these trace images subsequently used to measure grain size and grain aspect ratio. The metallographic image along with the superposed grain boundary trace for the sample examined here is given in Fig. 3. The mean grain diameter for the undeformed microstructure was quantified from the grain boundary trace image by measuring the average length of the diameters at two degree intervals for a line which passes through the grain centroid. The undeformed grain size distribution for this material based upon this measurement algorithm is given in Fig. 4a.

Granular aspect ratio was measured on both the undeformed material and on the sectioned shear zone of the deformed tophat sample (Ross, 2008). As with the grain size measurements, the aspect ratio measurements were made using the grain boundary trace images. The aspect ratio was measured manually from the digital

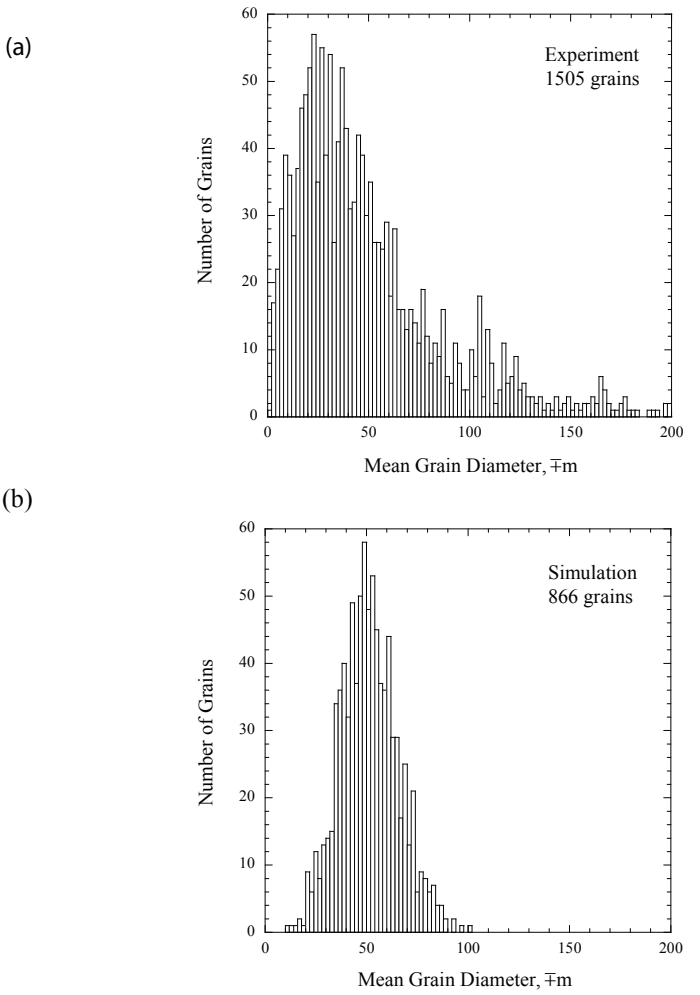

Figure 4: Grain size distributions (100 bins) as measured from (a) experimental metallographic and; (b) Voronoi tessellated microstructure used for all three realization simulations. Measurements made on the undeformed state.

images by first striking a line along the maximum dimension of the grain. The minor axis was then restricted to remain perpendicular with the major axis. The minor axis was placed at the location on the grain resulting in the maximum length of the minor axis. Measurements made on the deformed sample were tracked as a function of distance from the center of the shear zone and grains were chosen along lines at a fixed distance parallel with the center of the shear zone. The position of

these lines with respect to the cross-sectional image of the deformed sample can be found in Fig. 3b. Note that measurements were not taken along line I2-3. This resulted in granular aspect ratio data in eight bins; each at a different distance from the center of the shear zone. Aspect ratio data taken from the undeformed material can be found in Fig. 5a.

Granular aspect ratio data was used to approximate the equivalent tensile strain in each of the measured grains. Of course as the information given in Fig. 5a illustrates, based upon the measurement technique used by Ross (2008), the mean aspect ratio of the undeformed material was initially significantly greater than one (mean value of 1.9). Therefore our determination of strain from aspect ratio must take that initial state into account. In general, there will be an upper bound and lower bound to the value of strain evaluated. The upper and lower bounds in strain approximation come from the fact that we do not know the initial direction of the major axis of the grain in the undeformed configuration. If the major axis of the undeformed grain is aligned with the major axis of the deformed grain then the resulting strain is evaluated as a lower bound equivalent tensile strain and is given by

$$\varepsilon_l = \frac{2}{3} ln \left(\frac{AR}{\overline{AR}_0} \right) \tag{1}$$

where AR is granular aspect ratio and $\overline{AR}_0$ is the mean initial aspect ratio of the material as determined experimentally. On the other hand if the minor axis of the undeformed grain is aligned with the major axis of the deformed grain then the resulting strain is evaluated as an upper bound equivalent tensile strain and is given by

$$\varepsilon_u = \frac{2}{3} ln \left(AR \cdot \overline{AR}_0 \right). \tag{2}$$

All other initial granular alignments to the final deformed major axis will have equivalent tensile strain values between these two bounds. These relationships will be used later in our discussion of the results.

3 Single Crystal and Polycrystal Modeling

The constitutive and numerical models used here have been previously reported upon by Bronkhorst et al. (2007) and therefore only a brief outline of each is given here.

(a)

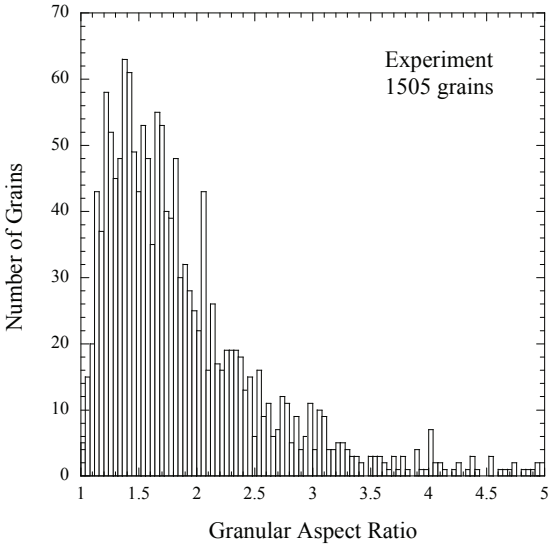

(b)

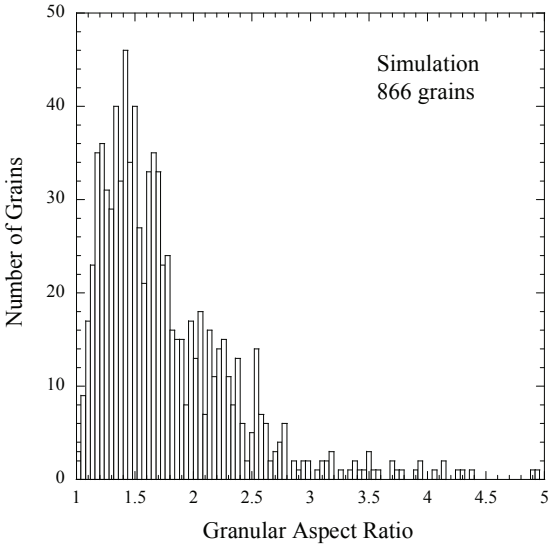

Figure 5: Granular aspect ratio distributions (100 bins) as measured from (a) experimental metallographic image and; (b) Voronoi tessellated microstructure. Measurements made on the undeformed state.

3.1 Single crystal constitutive model

The constitutive equation for the intragranular stress is taken as

$$T^* = \underline{C}[E^e - A(\theta - \theta_0)], \tag{3}$$

where $\underline{C}$ is the fourth order anisotropic crystal elasticity tensor, A is the second order crystal thermal expansion tensor, and θ_0 is the initial material temperature. This is the same relationship used by Kothari and Anand (1998). The elastic strain measure E^e is defined as

$$E^e \equiv \frac{1}{2}(F^{e^T} F^e - 1) \tag{4}$$

where the elastic deformation gradient is given by

$$F^e = F F^{p^{-1}}, \quad \det F^e > 0. \tag{5}$$

The measure of stress which is elastic work conjugate to the elastic strain measure E^e is defined by

$$T^* \equiv (\det F^e) F^{e^{-1}} T F^{e^{-T}}, \tag{6}$$

where T is the symmetric Cauchy stress. Based upon the work of Simmons and Wang (1971), the terms in the crystal elasticity tensor are made linearly temperature dependent by the following relationship

$$C_{ijkl} = C_{ijkl_0} + m_{C_{ijkl}} \theta \tag{7}$$

where C_{ijkl_0} are the appropriate values at 0K. The diagonal thermal expansion coefficient tensor for the crystal is given by

$$A_{ij} = \alpha_{ij} \delta_{ij}. \tag{8}$$

The plastic velocity gradient is related to the rate of slip on each of the crystallographic slip systems in the crystal $\dot{\gamma}^\alpha$, by the relationship

$$L^p = \dot{F}^p F^{p^{-1}} = \sum_\alpha \dot{\gamma}^\alpha S_0^\alpha, \quad S_0^\alpha \equiv m_0^\alpha \otimes n_0^\alpha, \tag{9}$$

where m_0^α and n_0^α are the vectors representing the slip direction and slip plane normal respectively for slip system α in the reference configuration. The flow rule

representing thermally activated slip rate on slip system α is given by a relationship introduced by Busso (1990)

$$\dot{\gamma}^{\alpha} = \dot{\gamma}_0 \exp\left[-\frac{F_0}{k\theta}\left\langle 1 - \left\langle \frac{|\tau^{\alpha}| - s_{\rho}^{\alpha}\frac{\mu}{\mu_0}}{s_{l}^{\alpha}\frac{\mu}{\mu_0}} \right\rangle^{p} \right\rangle^{q}\right] sgn(\tau^{\alpha}), \tag{10}$$

where s_{ρ}^{α} is the deformation resistance of slip system α due to evolving dislocation density and s_{l}^{α} is the constant intrinsic lattice resistance on slip system α. The magnitudes of each of these two quantities is defined at 0 K. Temperature sensitivity of the deformation resistances in Eq. (10) is represented to first order by scaling each quantity by the shear modulus ratio

$$\frac{\mu}{\mu_0} \cong \frac{C_{12}}{C_{12_0}} = 1 + \frac{m_{12}}{C_{12_0}}\theta. \tag{11}$$

The resolved shear stress drives the shear rate and is defined by the relationship

$$\tau^{\alpha} \equiv (C^{e}T^{*}) \cdot S_{0}^{\alpha}, \quad C^{e} = F^{e^{T}}F^{e}. \tag{12}$$

The evolution equation for the slip system deformation resistance is given by

$$\dot{s}_{\rho}^{\alpha} = \sum_{\beta} h^{\alpha\beta}\left|\dot{\gamma}^{\beta}\right|. \tag{13}$$

The total hardening rate which includes the effects of forest hardening is taken as

$$h^{\alpha\beta} = \left[r + (1-r)\delta^{\alpha\beta}\right]h^{\beta}. \tag{14}$$

The self-hardening rate h^{β} used here is that introduced by Acharya and Beaudoin (2000) which includes effects of both dislocation generation and annihilation is given by

$$h^{\beta} = h_o\left(\frac{s_s^{\beta} - s_{\rho}^{\beta}}{s_s^{\beta} - s_0^{\beta}}\right), \tag{15}$$

where the saturation stress parameter s_s^{β} as a function of temperature and shear rate, as proposed by Kocks (1976), is given as

$$s_s^{\beta} = \hat{s}_s^{\beta}(\dot{\gamma}, \theta) = s_{s_0}\left(\frac{\dot{\gamma}^{\beta}}{\dot{\gamma}_0}\right)^{\frac{k\theta}{A}} \tag{16}$$

For the high rate applications examined here, adiabatic conditions were assumed where the relationship between plastic work and temperature is given by

$$\rho c_p \dot{\theta} = \eta \sum_{\alpha} \tau^{\alpha} \dot{\gamma}^{\alpha}, \tag{17}$$

where $\eta \in [0,1]$ is the conversion efficiency factor, taken here as 0.95 for dynamic conditions. Values of material parameters used in the calculations presented here can be found in Bronkhorst et al. (2007).

3.2 Numerical Model and Polycrystal Shear Zone

Numerical simulations of the forced shear experiment were performed using an embedded polycrystal region within the shear zone of an axi-symmetric model. As described in detail by Bronkhorst et al. (2007), this region is constructed by Voronoi tessellation to an average grain size of 37 microns. The polycrystal shear zone contains 1091 grains. Their individual initial crystallographic orientation was represented by a set of 512 orientations which were chosen based upon orientation image mapping measurements of the undeformed material and represent the initially textured state. Three replicate sets of these 512 orientations were combined and individual orientations were randomly selected in order to assign the initial orientation to the 1091 grains. Three realizations of initial crystallographic orientation were produced through three different randomizations of the set of 3×512 orientations. The topology of the tessellation representing the microstructure in the shear zone geometry can be found in Fig. 6. The relationship between the microstructure of Fig. 6 and complete simulated geometry can be found in Fig. 7. Grain size and aspect ratio was measured on this tessellation using the same technique as that for the experimental measurement and their results are given in Figs. (4b) and (5b). Note that a single tessellation was used for each of the three realization calculations. Each grain was subdivided into three-noded triangular elements with approximately 50 elements representing an average sized grain.

Outside of the shear zone, the material does not experience strain in excess of 0.05 and so a simple small-strain J2 flow theory with the strain-rate dependent response represented by the isotropic Mechanical Threshold Stress (MTS) model (Follansbee and Kocks (1988); Chen and Gray (1996); and Maudlin et al. (1999)) is used. A schematic representation of the numerical model can be found in Fig. 7. Prescribed displacement conditions are applied equally to all nodes of the top loading surface. A constant velocity was applied to the top surface, the value of which was evaluated from the slope of the straight line segment of the displacement time curve given in Fig. 2 to a target total displacement of 0.4 mm. The base surface is assumed to be rigid and frictionless. The two inside corners are frictional contact

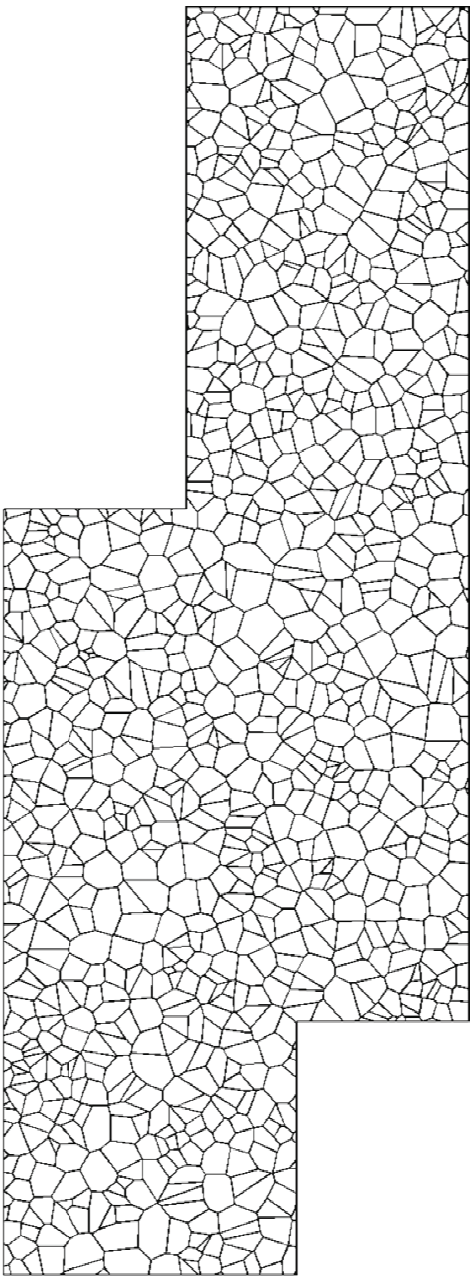

Figure 6: Voronoi tessellated polycrystal region used to represent the two-dimensional shear zone. This microstructure was embedded in a numerical model representing the entire sample illustrated in Fig. 7.

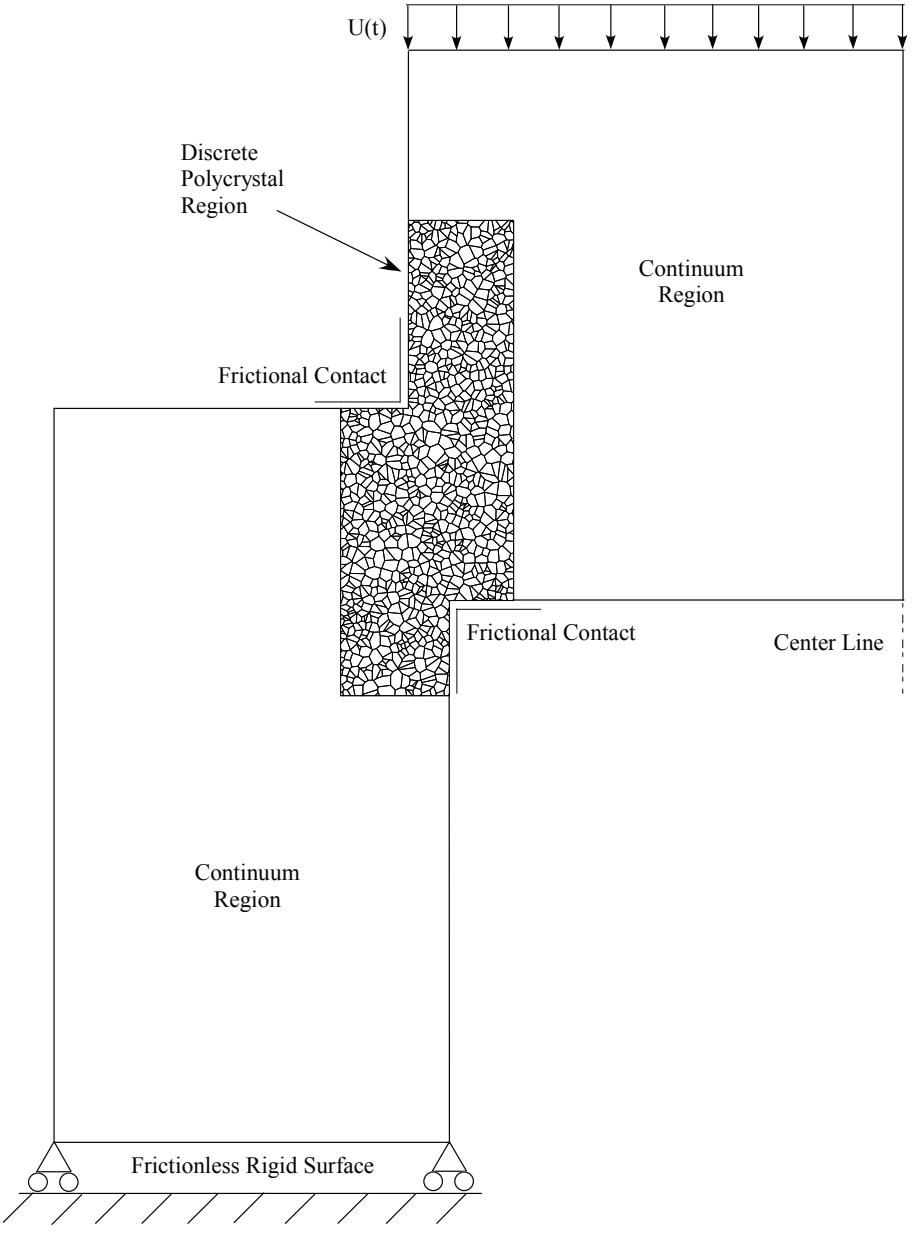

Figure 7: Numerical model used to represent the axisymmetric forced shear sample. The shear zone region is represented by a direct polycrystal representation.

surfaces and following Bronkhorst et al. (2006), a constant friction coefficient of 0.2 was used. The finite element code ABAQUS (2005) was used for these simulations.

4 Simulation and Experimental Results

The top surface stress versus displacement from simulation of the three crystallographic realizations are given in Fig. 8 along with that of the experiment. Since it is not practical to model the entire Split-Hopkinson Pressure Bar system, the oscillations in stress as experienced experimentally are not predicted. In general the models over-predict the stress response of the material for this type of loading. The most likely explanation for this is that the 2D simulations impose a degree of restraint on the deformation response of the polycrystal aggregate and therefore this restraint artificially increases the stress response. The thermal coupling contained in Eqs. (3), (7), (10), (11), (16), and (17) produce temperatures in the shear zone which are consistent with continuum calculations which do reasonably predict the stress response observed experimentally (Bronkhorst et. al, 2006). But of course it is not possible to experimentally confirm the accuracy of the temperature evolution in the axi-symmetric sample so this also remains a possible explanation for this stress response discrepency.

Results of deformed sample grain aspect ratio measurements are given in Fig. 9 as a function of the distance from the shear zone center as per the metallographic section and positions given in Fig. 3. Measurements on the undeformed material far from the shear zone reported by Ross (2008) indicate a mean initial aspect ratio of 1.9. The measurement results in Fig. 9 indicate a significant degree of variability in the measured grain aspect ratio at any given position. Mean aspect ratio is also plotted in Fig. 9 and indicates that their magnitude returns to those of the undeformed state within a distance of 0.2 mm on each side of the shear zone center.

As discussed earlier, the granular aspect ratio measurements were used to arrive at an approximate measure of strain in the shear zone using Eqs. (1) and (2) for upper and lower bound estimates. Equivalent plastic strain as a function of distance from the shear zone center was also calculated from the three numerical simulations. The schematic in Fig. 10 illustrates the region in which the material point information was taken from the numerical results after deformation. Contours of actual numerical results are given in Fig. 11. This rectangular region for each of the three simulations was chosen so that the long side was parallel with the line connecting the original corner points of the sample (shown as dots in Fig. 10). The ends of the rectangle were positioned inside the original corner points of the forced shear specimen by a distance 10% of the length between the original corner points. Note that with deformation, the corners collapse and contact occurs between the

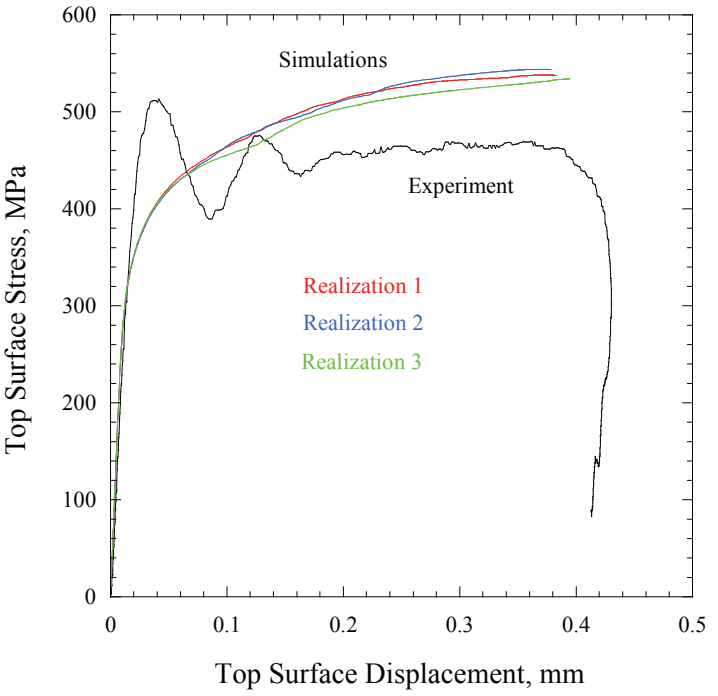

Figure 8: Top surface stress response comparison between the experimental result and the simulations of the three crystallographic realizations.

two sides of each corner. On average, 12,350 materials points are contained within each rectangle of width $\pm$ 0.2 mm from the shear zone center line. Equivalent plastic strain contour plots for all three realizations are given in Fig. 11.

Comparison between the experimental granular aspect ratio derived strain measurements (the solid black lines, using Eqs. (1) and (2)) and the plastic strain results of the three numerical simulations (the 12,350 red points) are given in Figs. 12 a-c. The dashed lines in Fig. 12 a-c indicate the curve of one standard deviation of the aspect ratio measurements from both the upper and lower bound strain curves. Note that in order to preserve the readability of the figures, only the Upper bound plus one standard deviation is plotted and the lower bound minus one standard deviation is plotted. The numerical results for all three realization simulations follow reasonably closely the lower bound experimental results.

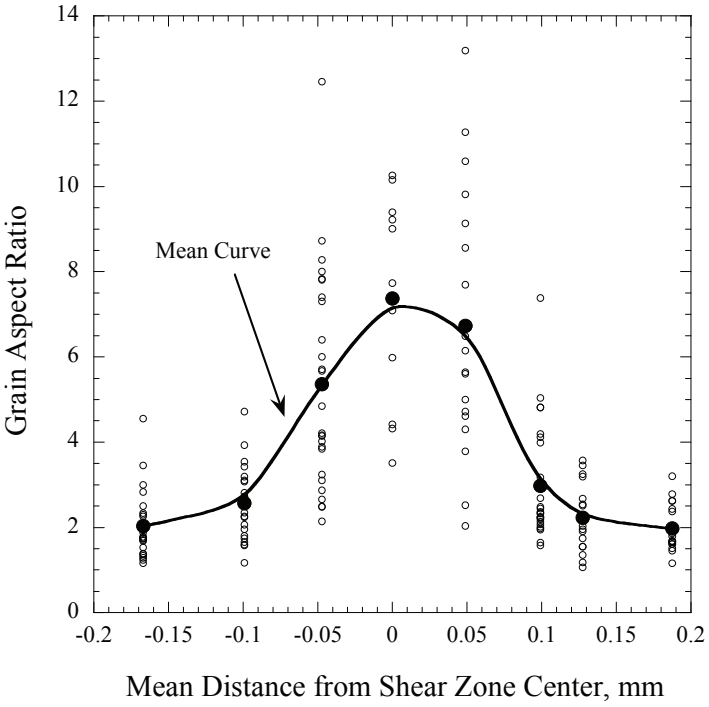

Figure 9: Results of granular aspect ratio measurements made on the digitized metallographic image in Fig. 3b (Ross, 2008). The filled points represent the mean aspect ratio value at each shear zone position. Negative position values indicate points nearest to the center of the axi-symmetric sample.

5 Discussion

This study is a continuation of the work of Bronkhorst et al. (2007) and provides direct comparison between local measurements of microstructural deformation and numerical simulations of simulated polycrystal aggregates. The measurements are unique in that they attempt to quantify the deformation field of the material inside the sample as opposed to measurements made on an exposed sample surface. The experimental measurements derived the strain measures at the length scale of the single crystal (40 μm) while those of the numerical simulations produced strain information at sub-grain length scales (7 μm). The numerical elements were chosen to be as small as possible but substantially larger than a typical dislocation subcell which for these deformed samples was on the order of 400 nm and is not represented by the constitutive model. The measurements were also made on only one

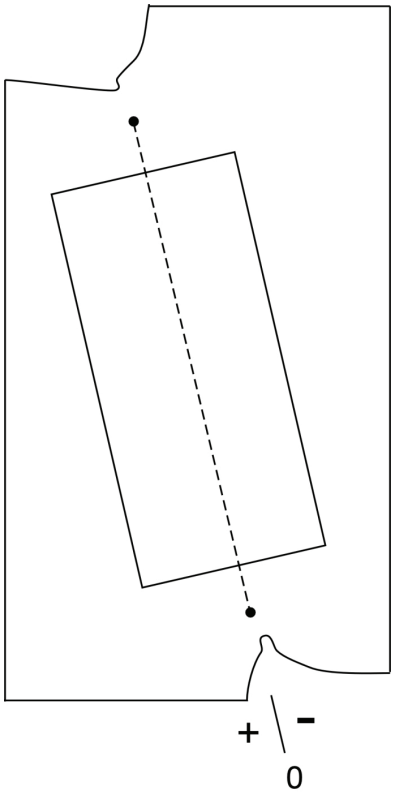

Figure 10: Schematic of the region from which equivalent strain information was extracted from the results of each of the three numerical simulations.

section of the material. One would expect that a different metallographic section would produce results which would be somewhat different. It would be interesting to quantify this difference.

The mean grain diameter comparisons given in Fig. 4 and the granular aspect ratio comparisons given in Fig. 5 offer interesting insight. The same measurement algorithm was used to derive both the experimental and simulated microstructure distributions. Although the mean grain size was the sole target for construction of the synthetic microstructures and these are represented reasonably well, the overall distribution of grain size is not represented well. On the other hand, the synthetic microstructure does a reasonably good job of representing the aspect ratio distribution observed experimentally. In the future if our interest is in numerical representing the extreme events such as localization, damage, and failure, it will be important to accurately represent the topological statistics of the material mi-

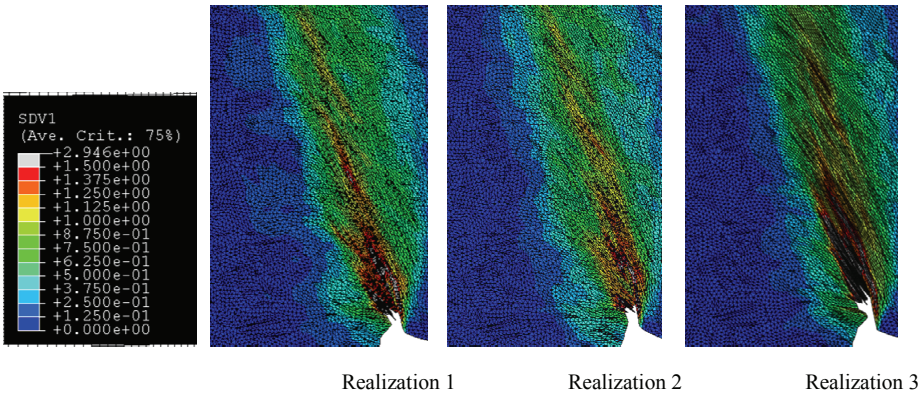

Figure 11: Contour plots showing equivalent plastic strain at the end of each simulation for each of the three crystallographic realizations.

crostructure accurately.

The granular aspect ratio measurements given in Fig. 9 suggest a high degree of variability at each position with respect to the shear zone center. The mean coefficient of variation for all positions is 0.38 with a minimum value of 0.27 and a maximum of 0.45. Although there are significantly fewer measurements at the center position as compared with the others, there is some indication that the variability is larger with the higher levels of deformation. The derivation of strain from aspect ratio measurements adds uncertainty to the results simply due to the fact that it is impossible to know the original morphology of the measured grains. This uncertainty is quantified in Fig. 12 through the upper and lower bound analysis. The approximation for the range of statistically possible values for strain at any given position can be considered to be between the two dashed curves in Fig. 12. While the upper bound and lower bound curves represent the uncertainty in initial grain morphology, the dashed curves add the variability quantified through the aspect ratio measurements.

Inherent in using a two-dimensional image to quantify strain is the assumption that the deformation was two-dimensional. Although impossible to quantify, this is likely another source of uncertainty in the measures of strain presented here. One would expect that even for a macroscopically axi-symmetric situation as exists here, the local deformation field would be three-dimensional in nature. Further work is necessary to understand to what degree this is true. It is likely that this would also depend upon the degree of crystallographic symmetry of the material. Even though the strain calculations from granular aspect ratio measurements assume two

(a)

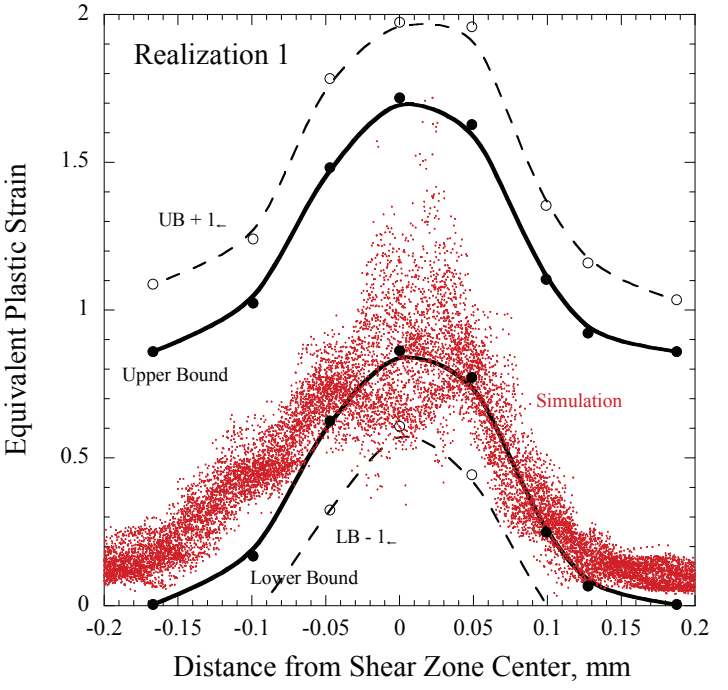
Realization 1
UB + 1
Upper Bound
Simulation
LB - 1
Lower Bound
Equivalent Plastic Strain
Distance from Shear Zone Center, mm
2
1.5
1
0.5
0
-0.2
-0.15
-0.1
-0.05
0
0.05
0.1
0.15
0.2

(b)

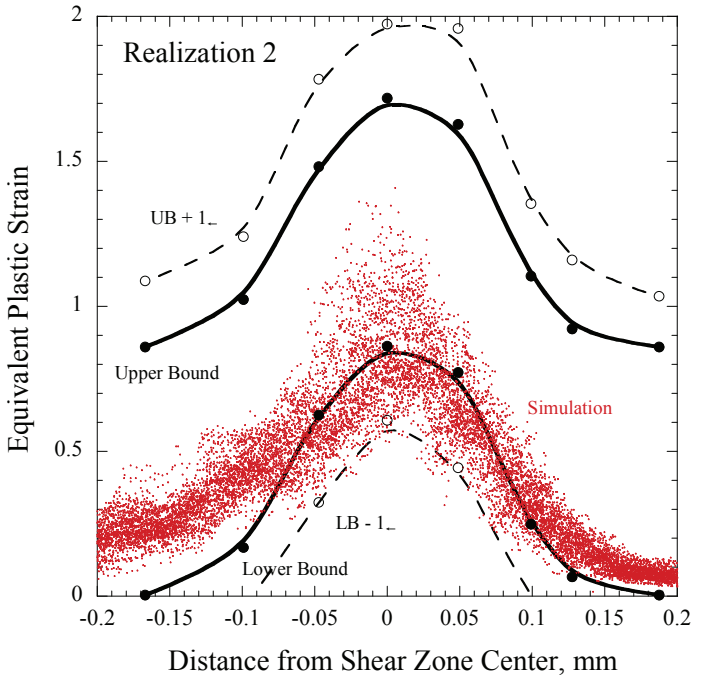
Realization 2
UB + 1
Upper Bound
Simulation
LB - 1
Lower Bound
Equivalent Plastic Strain
Distance from Shear Zone Center, mm
2
1.5
1
0.5
0
-0.2
-0.15
-0.1
-0.05
0
0.05
0.1
0.15
0.2

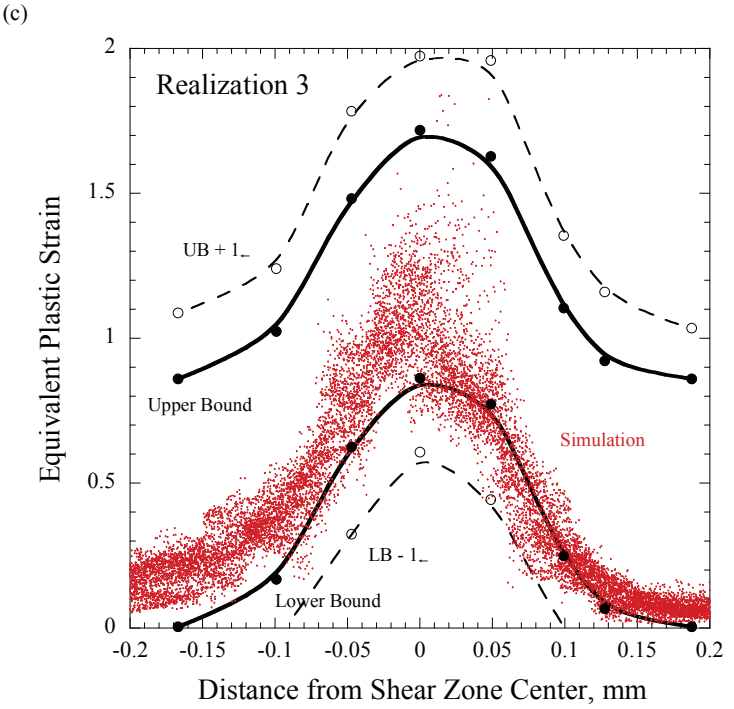

Figure 12: Comparison of the results of realization (a) 1; (b) 2; (c) 3 simulations to the strain evaluated from grain aspect ratio measurements. Negative position values indicate points nearest to the center of the axi-symmetric sample. The solid curves represent the mean lower and upper bound equivalent plastic strain evaluated from the metallographic images. The dashed curves represent the one standard deviation envelope around the experimental lower and upper bound curves. The red points represent the numerical results from all material points within the extracted shear zone region illustrated schematically in Fig. 10.

dimensional deformation, this is consistent with the numerical simulations included in this study. Certainly the single crystal constitutive model outlined in this paper is three-dimensional and must allow for slip to occur out of the plane, however the resultant strain is restricted at each material point to remain two-dimensional.

Given the strain measurement uncertainty discussed above, the results of the three numerical simulations based upon three different crystallographic orientation realizations compare favorably with the data as shown in Fig. 12. In all three cases, the numerical results consistently follow the experimental profile demonstrated by both lower and upper bound curves and are consistent in magnitude to the lower bound.

It should also be stated that because of mesh distortion causing convergence difficulties, neither of the three simulations achieved the total top surface displacement reached experimentally (0.42 mm). Therefore the simulation profiles in Fig. 12 are slightly lower in strain from what would have been achieved at full displacement and may explain the close match to the lower bound curve.

This work presenting comparisons between simulations of aggregate crystalline material and experimental measurements highlights many of the difficulties associated with these types of comparisons. Foremost among these is the lack of three-dimensional information both experimentally and computationally. Traditional experimental measurements by nature are generally performed on two-dimensional surfaces. Computational methods are also frequently done two-dimensionally due to problems meshing and characterizing complex three-dimensional structures. Thus, the effects of the third dimension are a source of uncertainty. It is also important to recognize that most experimental measurements are done post-mortem, giving only information in the final deformed state. Thus, comparisons are only available at the final state and not the initial or intermediate material states. The last difficulty encountered in comparing experimental and simulation information is the difference between simulated state variables and experimental measurements, e.g. a final deformation vs. strain or micro-indentation resistance vs. evolved critical resolved shear stress. It should be noted that most of these difficulties are current research topics being pursued within the materials community. This work gives an example for the need for such advances.

6 Conclusion

This study has employed a coupled thermo-viscoplastic single crystal constitutive model of tantalum together with a Voronoi tessellation based synthetic microstructure to represent the shear region of a forced shear sample. Granular aspect ratio measurements of the recovered sample cross section made by Ross (2008) were analyzed and used to estimate the strain within the shear zone of the sample. These were compared directly with the numerical simulations and found to compare reasonably well. Both experiments and calculations suggest a high degree of spatial variability in the local strain field. This variability is believed to be an important driver for damage and failure processes occurring under dynamically loaded conditions and therefore it is equally important to understand and quantify this linkage. As this study points out, there is still much work to do in both our ability to theoretically represent aggregate material response and also in our ability to experimentally probe the nucleation of damage events due to material variability.

Acknowledgement: This work was conducted under both the DoE Advance

Simulation and Computing Program and the joint DoD/DoE Munitions Technology Development Program.

7 References

ABAQUS (2005): Version 6.5-4 User's Manual. Providence RI. SIMULIA Inc.

Acharya, A., Beaudoin, A. J. (2000): Grain-size effect in viscoplastic polycrystals at moderate strains. *J. Mech. Phys. Solids* 48, 2213-2230.

Addessio, F. L., Johnson, J. N. (1993): Rate-dependent ductile failure model. *J. Appl. Phys.* 74, 1640-1648.

Barton, N. R., Bernier, J. V., Edmiston, J. K. (2009): Bringing together computational and experimental capabilities at the crystal scale. in press: Proceedings of the Conference of the American Physical Society Topical Group on Shock Compression of Condensed Matter, AIP, 2009.

Bronkhorst, C. A., Cerreta, E. K., Xue, Q., Maudlin, P. J., Mason, T. A., Gray III, G. T. (2006): An experimental and numerical study of the localization behavior of tantalum and stainless steel. *Int. J. Plasticity* 22, 1304-1335.

Bronkhorst, C. A., Hansen, B. L., Cerreta, E. K., Bingert, J. F. (2007): Modeling the microstructural evolution of metallic polycrystalline materials under localization conditions. *J. Mech. Phys. Solids* 55, 2351-2383.

Busso, E. P. (1990): Cyclic deformation of monocrystalline nickel aluminide and high temperature coatings, Ph.D. Thesis, MIT.

Chen, S. R., Gray III, G. T. (1996): Constitutive behavior of tantalum and tantalum-tungsten alloys. *Met. Mat. Trans.* A 27A, 2994-3006.

Cheong, K.-S., Busso, E. P. (2004): Discrete dislocation density modelling of single phase FCC polycrystal aggregates. *Acta Mater.* 52, 5665-5675.

Cheong, K.-S., Busso, E. P. (2006): Affects of lattice misorientations on strain heterogeneities in FCC polycrystals. *J. Mech. Phys. Solids* 54, 671-689.

Clayton, J. D., McDowell, D. L. (2003): A multiscale multiplicative decomposition for elastoplasticity of polycrystals. *Int. J. Plasticity* 19, 1401-1444.

Clayton, J. D., Schroeter, B. M., McDowell, D. L., Graham, S. (2002): Distributions of stretch and rotation in polycrystalline OFHC Cu. *ASME J. Engr. Mats. Tech.* 124, 302-313.

Czarnota, C., Jacques, N., Mercier, S., Molinari, A. (2008): Modeling of dynamic ductile fracture and application to the simulation of plate impact tests on tantalum. *J. Mech. Phys. Solids* 56, 1624-1650.

Delaire, F. (1999): Ph.D. Thesis, Universit Paris-Nord, France.

Follansbee, P. S., Kocks, U. F. (1988): A constitutive description of the deformation of copper based on the use of the mechanical threshold stress as an internal state variable. *Acta Metall.* 36, 81-93.

Gurson, A. L. (1977): Continuum theory of ductile rupture by void nucleation and growth: Part 1 – Yield criteria and flow rules for porous ductile media. *J. Eng. Mat. Tech.* 99, 2-15.

Haghi, M. (1995): A framework for constitutive relations and failure criteria for materials with distributed properties, with application to porous viscoplasticity, *J. Mech. Phys. Solids* 43, 573-597.

Kalidindi, S. R., Bhattacharyya, A., Doherty, R. D. (2004): Detailed analyses of grain-scale plastic deformation in columnar polycrystalline aluminum using orientation image mapping and crystal plasticity models. *Proc. R. Soc. Lond.* A 460, 1935-1956.

Kocks, U. F. (1976): Laws for work-hardening and low-temperature creep. *J. Eng. Mats. Tech.* 98, 76-85.

Kothari, M, Anand, L. (1998): Elasto-viscoplastic constitutive equations for polycrystalline metals: application to tantalum. *J. Mech. Phys. Solids* 46, 51-83.

Lebensohn, R. A. (2001): N-site modelling of a 3D viscoplastic polycrystal using the fast Fourier transform. *Acta Mater.* 49, 2723-2737.

Lebensohn, R. A., Tomé, C. N. (1993): A self-consistent anisotropic approach for the simulation of plastic deformation and texture development of polycrystals: application to zirconium alloys. *Acta Metall.* Mater. 41, 2611-2624.

Lebensohn, R. A., Ponte Castaeda, P., Idiart, M. I., Vincent, P.-G., Tom, C. N. (2009): Dilatational viscoplasticity of polycrystalline materials. To be submitted to *J. Mech. Phys. Solids*.

Leblond, J. B., Perrin, G., Sequet, P. (1994): Exact results and approximate models for porous viscoplastic solids. *Int. J. Plasticity* 10, 213-235.

Maudlin, P. J., Bingert, J. F., House, J. W., Chen, S. R. (1999): On the modeling of the Taylor cylinder impact test for orthotropic textured materials: experiments and simulations. *Int. J. Plasticity* 15, 139-166.

Ross, A. R. (2008): Characterization of shear localization microstructures generated by forced shear experiments. Master of Science Thesis, New Mexico Institute of Mining and Technology, December.

Schroeter, B. M., McDowell, D. L. (2003): Measurement of deformation fields in polycrystalline OFHC copper. *Int. J. Plasticity* 19, 1355-1376.

Simmons, G., Wang, H. (1971): Single crystal elastic constants and calculated aggregate properties: A handbook. The M.I.T. Press, Cambridge, MA.

Tong, W., Ravichandran, G. (1995): Intertial effects on void growth in porous viscoplastic materials., *ASME J. Appl. Mech.* 62, 633–639.

Tvergaard, V. (1981): Influence of voids on shear band instabilities under plane strain conditions, *Int. J. Fracture* 17, 389-407.

Tvergaard, V. (1982): On localization in ductile materials containing spherical voids, *Int. J. Fracture* 18, 237-252.

Tvergaard, V., Needleman, A. (1984): Analysis of the cup-cone fracture in a round tensile bar, *Acta Metall.* 32, 157-169.

Vogler, T. J., Clayton, J. D. (2008): Heterogeneous deformation and spall of an extruded tungsten alloy: plate impact experiments and crystal plasticity modeling, *J. Mech. Phys. Solids* 56, 297-335.

Weinberg, K., Mota, A., Ortiz, M. (2006): A variational constitutive model for porous metal plasticity. *Comput. Mech.* 37, 142-152.

Zavaliangos, A., Anand, L. (1993): Thermo-elasto-viscoplasticity of isotropic porous metals. *J. Mech. Phys. Solids* 41, 1087-1118.

Zhang, N., Tong, W. (2004): An experimental study on grain deformation and interactions in an Al-5%Mg multicrystal. *Int. J. Plasticity* 20, 523-542.